

The young massive stellar cluster associated to RCW121

A. Roman-Lopes¹ and Z. Abraham¹

ABSTRACT

We report NIR broad and narrow band photometric observations in the direction of the IRAS17149-3916 source that reveal the presence of a young cluster of massive stars embedded in an HII region coincident with RCW121. These observations, together with published radio data, MSX and Spitzer images were used to determine some of the physical parameters of the region. We found 96 cluster member candidates in an area of about 1.5×2.0 square arcmin, 30% of them showing excess emission in the NIR. IRS 1, the strongest source in the cluster with an estimated spectral type of O5V-O6V ZAMS based on the color-magnitude diagram, is probably the main ionizing source of the HII region detected at radio wavelengths. Using the integrated Br γ and the 5 GHz flux densities, we derived a mean visual extinction $A_V = 5.49 \pm_{1.32}^{2.06}$ magnitudes. From the observed size of the Br γ extended emission, we calculated the emission measure $E = 4.5 \times 10^{24} \text{cm}^{-5}$ and the electron density $n_e = 2.6 \times 10^3 \text{cm}^{-3}$, characteristic of compact HII regions.

Subject headings: stars : formation – stars: pre-main sequence – infrared : stars – ISM: HII regions – ISM: dust, extinction

1. Introduction

Young massive stars are found inside dense molecular clouds generally suffering high extinction at optical wavelengths, mainly due to the large amount of gas and dust remaining from the star forming process (Churchwell 1990; Cesaroni 1991). Color-color and color-magnitude diagrams from near infrared photometry (NIR) allow the determination of the reddening of each individual star (at least for those that do not present intrinsic excess emission in the NIR). Longslit K -band spectra have shown that a large number of those NIR sources present broad Br γ emission and no photospheric features (Armand et al. 1996; Hanson, Luhman & Rieke 2002), typical of very young pre-main sequence stars surrounded by disks and/or cocoons (Churchwell 1990).

On the other hand, narrow band imaging observations of star forming regions (e.g. centered in the Br γ line and in the adjacent continuum) are powerful tools to study the emission from the extended surroundings. In fact, by comparing the Br γ flux density with the free-free radio emission,

¹Instituto de Astronomia, Geofísica e Ciências Atmosféricas, Universidade de São Paulo
Rua do Matão 1226, 05508-900, São Paulo, SP, Brazil

it is possible to estimate the absorption (Hanson, Luhman & Rieke 2002). Moreover, using the measured size of the Br γ emitting region and the low resolution radio flux density, it is possible to obtain the emission measure and mean value for the electron density (Mezger & Henderson 1967). We have to take into account that the measured size of the Br γ emitting region is limited by the sensitivity of the NIR detector systems. The recent near to mid infrared images obtained by the Spitzer space telescope ¹, represent an additional constrain to the size of the ionized region, since they delineate the dusty border of the HII region.

RCW121 located at $l=348^{\circ}2$ and $b=-1^{\circ}0$ (Rodgers, Campbell & Whiteoak 1960) is a strong (11.9 Jy) and compact (about 1 arcmin angular diameter) 5 GHz continuum source (PMNJ 1718-3916), observed in the H109 α and H110 α recombination lines by Caswell & Haynes (1987). The CS(2-1) transition, typical of dense molecular clouds, was also detected by Bronfman, Nyman & May (1996) and methanol maser emission at 6.7 GHz, generally associated to high mass stellar forming regions, was observed with the Parkes radio telescope by Walsh et al. (1997). Maser emission from excited OH in the $^2\Pi_{1/2}$ J=1/2 state was found by Cohen, Mashedier & Caswell (1995) at all three transitions (4765, 4750 and 4660 MHz). Dutra et al. (2003), by visual inspection of 2MASS images, found a cluster of stars in the direction of RCW121; this fact, together with the presence of an IRAS source with colors of compact HII regions (Wood & Churchwell 1989) indicates that star formation has recently occurred. Despite of the overwhelming evidences pointing to the existence of young and massive stellar objects associated with RCW121, no detailed studies of the stellar content of the region were made up to the present.

This work is part of a larger survey (Roman-Lopes et al. 2003; Roman-Lopes & Abraham 2004a,b), aimed at the detection of the exciting stars of compact HII regions associated with IRAS point sources which are also strong CS emitters (Bronfman, Nyman & May 1996). In the next sections we present the results of NIR broad and narrow band photometric observations of a young cluster of massive stars found in the direction of the IRAS17149-3916 source. In Section 2 we describe the NIR observations; in Section 3 we present the results from the broad and narrow band NIR filters and in Section 4 we summarize the work.

2. Observations and data reduction

The NIR imaging photometric observations were performed in 2003 May in the direction of IRAS point source 17149-3916, using the near infrared camera of the Laboratório Nacional de Astrofísica, Brazil, mounted on the 0.6 m Boller & Chivens (BC) telescope; the resulting plate scale of the images is $0.48''\text{pixel}^{-1}$. The images were made using the J and H broad band filters and the K narrow band filter $C1$, centered at $2.14\mu\text{m}$ continuum. Since meaningful information about the ionized regions can be obtained from narrow band Br γ images (Roman-Lopes & Abraham

¹<http://irsa.ipac.caltech.edu/Missions/spitzer.html>

2005), we also made observation in 2005 May, using the near infrared camera, mounted on the 1.6 m Perkin-Elmer (PE) telescope; the resulting plate scale of the images is $0.24'' \text{ pixel}^{-1}$.

The observations (mean FWHM values of the point-spread functions, the total integration times, etc) are summarized in Table 1. The NIR images were reduced using programs within the IRAF image reduction package system. Each image was corrected for nonlinear response, dark-subtracted, flattened, and masked to eliminate bad pixels. We observed calibration stars from the list of 2MASS standards at similar air mass of our science targets. In addition we checked our photometric results by comparing it with the 2MASS photometry for common bright field stars. Details about the calibration and reduction procedures can be found in Roman-Lopes et al. (2003).

3. Results

Figure 1 shows the J , H and K near infrared images obtained during the 2003 observing run (upper, central and lower panels, respectively).

3.1. The stellar cluster

To separate the cluster population from the field stars we analyzed the stellar colors in two distinct areas as can be seen in Figure 1: one, labeled "cluster" and measuring about $2.2' \times 2.4'$, encloses the IR nebula; the other, labeled "control" and measuring about $8.8' \times 1.3'$, includes the eastern and southern parts of the images. From the $(J - H)$ versus $(H - K)$ comparative diagrams, shown in Figure 2, we can see that a significant number of "cluster" sources have excess emission at the longer wavelengths, probably due to the presence of warm circumstellar dust or disks (Lada & Adams 1992). On the other hand, the majority of the sources in the "control" diagram lie inside the reddening band for the Galactic field stars. They can be divided in two groups separated by a gap around $(J - H) \sim 1.4$: the first is formed by foreground field stars while the other is composed probably by giants stars located behind the molecular cloud.

Table 1. Summary of the NIR observations

Filter	Date	Telescope	ITIME	FWHM(")
J	May 2003	BC ²	840	1.9
H	May 2003	BC	420	2.0
$K(C1)$	May 2003	BC	7200	2.1
$K(\text{Br}\gamma)$	May 2005	PE ³	360	1.7
$K(C1)$	May 2005	PE	360	1.7

¹ Boller & Chivens 0.6 m telescope

² Perkin & Elmer 1.6 m telescope

We assumed as candidate cluster members all NIR sources that lie along the early type reddening band and those showing excess emission in the "cluster" color-color diagram. For the infrared sources not detected in the J band a different criteria had to be used. In order to distinguish the genuine candidate cluster members from the field stars, we analyzed for the two selected areas, the number of stars $N(H - K)$ with $(H - K)$ colors as a function of $(H - K)$. The results with the counts normalized to the cluster region area are shown in Figure 3; we can see in the cluster area an excess of counts in the color ranges $(H - K) \sim 0 - 0.75$ and $(H - K) \geq 1$. The first range corresponds to the cluster sources and the second group can be formed either by genuine cluster members or by giant stars located behind the molecular cloud. For this reason, only six stars not detected in the J band, with colors $(H - K) \sim 0 - 0.75$ or $(H - K) \geq 1$ and located inside the nebula region were taken as candidates cluster members.

In Figure 4, we show the K band contour diagram in which the relative position of each selected source is indicated. There, we show the objects that present excess emission in the NIR (filled triangles), those without (open triangles), as well as the sources detected only in the H and K bands (filled squares).

We assumed a kinematic distance to the cluster of 1.6 kpc (Walsh et al. 1997), for a galactocentric distance of 8.5 kpc. Using this value, the luminosity of the stars in Table 2 can be inferred from the J versus $(J - H)$ color-magnitude diagram shown in Figure 5. The position of the main-sequence is plotted together with each spectral type earlier than F8V. The intrinsic colors were taken from Koornneef (1983) and the absolute J magnitudes were computed from the absolute visual luminosity for ZAMS given by Hanson et al. (1997). The reddening vector for a ZAMS B0 V star, as in Fitzpatrick (1999), is shown by the dashed line together with the positions of visual extinction $A_V = 10, 20$ and 30 magnitudes indicated by filled circles.

From the color-magnitude diagram, we can see that IRS1, IRS5, IRS9 and IRS12 are the most luminous objects without excess emission in the whole region, being the best ionizing source candidates. An inspection of the relative position of these sources shows that only IRS1 is located in the central part of the infrared nebula; the others lie at the border of the extended emission region. In this sense IRS1, an O5V-O6V ZAMS from Figure 5, probably is the main source of Lyman continuum photons that are ionizing the HII region detected at radio wavelengths.

Table 2. List of the selected near-infrared sources

IRS	α (J2000)	δ (J2000)	J_{CamIV}	H_{CamIV}	K_{CamIV}
1	17:18:25.51	-39:19:08.8	8.93 \pm 0.02	8.36 \pm 0.02	8.02 \pm 0.02
2	17:18:25.73	-39:18:27.0	11.81 \pm 0.02	9.64 \pm 0.02	8.45 \pm 0.02
3	17:18:22.27	-39:18:42.5	11.60 \pm 0.02	10.23 \pm 0.02	9.06 \pm 0.02
4	17:18:22.92	-39:18:22.7	15.03 \pm 0.03	11.70 \pm 0.02	9.72 \pm 0.02
5	17:18:20.59	-39:18:07.2	11.87 \pm 0.03	10.66 \pm 0.02	10.06 \pm 0.02
6	17:18:30.72	-39:18:40.0	11.43 \pm 0.02	10.75 \pm 0.02	10.26 \pm 0.02
7	17:18:25.66	-39:19:09.8	11.61 \pm 0.03	10.86 \pm 0.03	10.32 \pm 0.04
8	17:18:26.62	-39:17:51.7	12.05 \pm 0.02	10.98 \pm 0.03	10.40 \pm 0.02
9	17:18:25.34	-39:18:24.8	13.53 \pm 0.03	11.47 \pm 0.02	10.42 \pm 0.02
10	17:18:25.32	-39:19:09.5	11.87 \pm 0.03	11.35 \pm 0.02	10.60 \pm 0.08
11	17:18:28.75	-39:19:15.6	11.23 \pm 0.02	10.96 \pm 0.02	10.69 \pm 0.03
12	17:18:30.36	-39:19:53.0	14.97 \pm 0.04	12.16 \pm 0.02	10.75 \pm 0.03
13	17:18:30.70	-39:19:52.7	11.52 \pm 0.03	11.12 \pm 0.02	10.86 \pm 0.03
14	17:18:25.39	-39:19:12.0	12.30 \pm 0.03	11.36 \pm 0.03	10.91 \pm 0.03
15	17:18:31.90	-39:19:40.4	12.27 \pm 0.03	11.33 \pm 0.03	10.93 \pm 0.03
16	17:18:32.04	-39:17:54.2	13.87 \pm 0.03	12.06 \pm 0.03	11.08 \pm 0.03
17	17:18:31.68	-39:18:24.1	12.28 \pm 0.03	11.48 \pm 0.03	11.13 \pm 0.03
18	17:18:25.18	-39:18:46.8	14.87 \pm 0.03	12.44 \pm 0.03	11.20 \pm 0.03
19	17:18:24.48	-39:19:39.7	11.70 \pm 0.03	11.43 \pm 0.03	11.22 \pm 0.03
20	17:18:22.42	-39:18:21.2	12.77 \pm 0.03	11.74 \pm 0.03	11.21 \pm 0.03
21	17:18:32.98	-39:19:32.2	12.04 \pm 0.03	11.58 \pm 0.03	11.27 \pm 0.03
22	17:18:25.75	-39:19:55.9	14.35 \pm 0.03	12.33 \pm 0.03	11.41 \pm 0.03
23	17:18:21.70	-39:19:15.2	14.78 \pm 0.03	12.66 \pm 0.03	11.45 \pm 0.03
24	17:18:21.60	-39:18:31.7	14.91 \pm 0.03	12.63 \pm 0.03	11.46 \pm 0.03
25	17:18:29.40	-39:17:56.0	12.30 \pm 0.03	11.78 \pm 0.03	11.47 \pm 0.03
26	17:18:30.91	-39:18:33.8	12.66 \pm 0.03	11.89 \pm 0.03	11.49 \pm 0.03
27	17:18:20.59	-39:18:13.0	12.02 \pm 0.03	11.72 \pm 0.03	11.50 \pm 0.03
28	17:18:22.44	-39:19:20.6	12.89 \pm 0.03	12.07 \pm 0.03	11.52 \pm 0.03
29	17:18:25.97	-39:19:26.8	13.48 \pm 0.03	12.29 \pm 0.03	11.59 \pm 0.03
30	17:18:26.16	-39:17:42.7	15.25 \pm 0.03	12.88 \pm 0.03	11.61 \pm 0.04
31	17:18:23.33	-39:19:08.0	13.45 \pm 0.03	12.35 \pm 0.03	11.76 \pm 0.03
32	17:18:31.37	-39:18:10.4	14.98 \pm 0.03	12.84 \pm 0.03	11.84 \pm 0.03
33	17:18:23.83	-39:19:04.4	12.98 \pm 0.03	12.31 \pm 0.03	11.86 \pm 0.03
34	17:18:29.69	-39:19:02.3	12.74 \pm 0.03	12.23 \pm 0.03	11.90 \pm 0.03
35	17:18:25.54	-39:19:23.2	13.55 \pm 0.03	12.48 \pm 0.03	11.90 \pm 0.03
36	17:18:29.81	-39:19:07.3	15.62 \pm 0.04	13.21 \pm 0.03	11.91 \pm 0.03
37	17:18:21.48	-39:19:13.8	13.05 \pm 0.03	12.39 \pm 0.03	11.92 \pm 0.03
38	17:18:27.89	-39:17:58.6	15.28 \pm 0.04	13.02 \pm 0.03	11.93 \pm 0.03
39	17:18:21.77	-39:19:22.1	15.36 \pm 0.05	13.24 \pm 0.03	11.93 \pm 0.03
40	17:18:24.48	-39:19:21.4	13.28 \pm 0.03	12.51 \pm 0.03	11.96 \pm 0.03
41	17:18:21.22	-39:18:38.5	14.86 \pm 0.04	13.13 \pm 0.04	12.01 \pm 0.05
42	17:18:25.87	-39:18:56.9	13.82 \pm 0.04	12.71 \pm 0.03	12.09 \pm 0.05
43	17:18:24.70	-39:18:41.8	12.71 \pm 0.04	12.25 \pm 0.03	12.03 \pm 0.05
44	17:18:25.30	-39:18:37.8	13.36 \pm 0.04	12.62 \pm 0.04	12.10 \pm 0.05
45	17:18:25.75	-39:19:25.3	13.77 \pm 0.04	12.81 \pm 0.04	12.14 \pm 0.05
46	17:18:22.90	-39:19:40.8	12.91 \pm 0.04	12.46 \pm 0.04	12.18 \pm 0.05

Table 2—Continued

IRS	α (J2000)	δ (J2000)	J_{CamIV}	H_{CamIV}	K_{CamIV}
47	17:18:23.33	-39:18:27.4	13.09 \pm 0.04	12.61 \pm 0.04	12.18 \pm 0.05
48	17:18:23.35	-39:18:56.2	13.32 \pm 0.04	12.68 \pm 0.04	12.34 \pm 0.05
49	17:18:24.48	-39:18:09.7	16.31 \pm 0.06	13.82 \pm 0.04	12.51 \pm 0.06
50	17:18:26.57	-39:19:03.4	13.13 \pm 0.04	12.79 \pm 0.04	12.55 \pm 0.06
51	17:18:24.14	-39:18:31.0	13.40 \pm 0.04	12.88 \pm 0.04	12.62 \pm 0.06
52	17:18:32.74	-39:18:14.0	12.83 \pm 0.04	12.45 \pm 0.04	12.33 \pm 0.05
53	17:18:23.28	-39:19:05.9	15.11 \pm 0.05	13.74 \pm 0.04	12.63 \pm 0.06
54	17:18:21.94	-39:18:41.4	14.64 \pm 0.04	13.37 \pm 0.04	12.66 \pm 0.06
55	17:18:32.88	-39:19:05.5	14.56 \pm 0.04	13.37 \pm 0.04	12.70 \pm 0.06
56	17:18:28.32	-39:19:49.8	14.73 \pm 0.04	13.46 \pm 0.04	12.71 \pm 0.06
57	17:18:23.47	-39:19:52.3	13.27 \pm 0.04	12.93 \pm 0.04	12.73 \pm 0.06
58	17:18:20.62	-39:19:55.2	13.59 \pm 0.04	13.06 \pm 0.04	12.80 \pm 0.06
59	17:18:24.74	-39:19:06.6	15.00 \pm 0.05	13.63 \pm 0.04	12.84 \pm 0.07
60	17:18:25.61	-39:19:16.7	14.58 \pm 0.04	13.31 \pm 0.04	12.65 \pm 0.06
61	17:18:24.43	-39:18:40.7	15.75 \pm 0.05	14.00 \pm 0.04	12.86 \pm 0.07
62	17:18:24.43	-39:19:23.5	15.87 \pm 0.07	14.70 \pm 0.04	12.94 \pm 0.08
63	17:18:24.48	-39:19:10.9	15.34 \pm 0.06	13.80 \pm 0.04	13.01 \pm 0.08
64	17:18:21.29	-39:18:51.1	14.42 \pm 0.04	13.40 \pm 0.04	12.98 \pm 0.08
65	17:18:30.58	-39:18:37.1	14.01 \pm 0.04	13.49 \pm 0.04	13.06 \pm 0.08
66	17:18:22.90	-39:18:59.0	15.18 \pm 0.04	13.81 \pm 0.04	13.11 \pm 0.08
67	17:18:23.52	-39:19:10.6	14.10 \pm 0.04	13.51 \pm 0.04	13.12 \pm 0.08
68	17:18:26.35	-39:19:18.5	14.73 \pm 0.04	13.64 \pm 0.04	13.15 \pm 0.08
69	17:18:21.05	-39:18:44.6	17.12 \pm 0.14	14.53 \pm 0.05	13.20 \pm 0.09
70	17:18:21.77	-39:18:48.2	13.80 \pm 0.04	13.42 \pm 0.04	13.26 \pm 0.09
71	17:18:26.86	-39:18:49.0	14.06 \pm 0.04	13.61 \pm 0.04	13.27 \pm 0.09
72	17:18:33.19	-39:18:13.7	13.59 \pm 0.04	13.27 \pm 0.04	13.11 \pm 0.08
73	17:18:23.28	-39:18:46.1	15.43 \pm 0.06	14.29 \pm 0.04	13.27 \pm 0.09
74	17:18:29.86	-39:19:28.9	14.48 \pm 0.04	13.76 \pm 0.04	13.31 \pm 0.09
75	17:18:27.14	-39:19:11.3	14.90 \pm 0.05	13.96 \pm 0.04	13.39 \pm 0.09
76	17:18:22.75	-39:18:45.4	15.85 \pm 0.06	14.49 \pm 0.05	13.32 \pm 0.09
77	17:18:19.94	-39:17:57.1	15.22 \pm 0.05	14.26 \pm 0.04	13.76 \pm 0.10
78	17:18:32.38	-39:19:10.9	17.01 \pm 0.08	14.97 \pm 0.06	13.34 \pm 0.09
79	17:18:22.75	-39:18:11.5	14.61 \pm 0.05	13.92 \pm 0.04	13.55 \pm 0.09
80	17:18:26.50	-39:19:32.9	14.54 \pm 0.05	13.95 \pm 0.04	13.65 \pm 0.10
81	17:18:22.18	-39:19:26.0	14.97 \pm 0.05	14.22 \pm 0.04	13.59 \pm 0.10
82	17:18:26.40	-39:19:06.6	17.02 \pm 0.13	15.67 \pm 0.05	14.27 \pm 0.16
83	17:18:23.33	-39:18:39.2	14.95 \pm 0.05	14.42 \pm 0.05	13.71 \pm 0.11
84	17:18:30.74	-39:19:14.5	15.45 \pm 0.05	14.65 \pm 0.04	13.75 \pm 0.10
85	17:18:31.15	-39:19:52.0	13.84 \pm 0.04	13.50 \pm 0.04	13.32 \pm 0.09
86	17:18:21.55	-39:19:48.0	15.31 \pm 0.05	14.42 \pm 0.05	13.82 \pm 0.11
87	17:18:28.94	-39:18:44.6	15.05 \pm 0.04	14.32 \pm 0.04	13.83 \pm 0.12
88	17:18:26.30	-39:19:50.2	14.67 \pm 0.04	14.24 \pm 0.05	14.01 \pm 0.13
89	17:18:22.42	-39:18:36.4	15.44 \pm 0.04	14.06 \pm 0.04	13.28 \pm 0.09
90	17:18:28.80	-39:19:54.1	14.33 \pm 0.04	13.95 \pm 0.04	13.88 \pm 0.11
91	17:18:30.48	-39:18:45.7		14.11 \pm 0.05	11.31 \pm 0.04
92	17:18:28.94	-39:19:21.7		13.25 \pm 0.03	11.34 \pm 0.04

3.2. The IRAS source

In Figure 6 we show the K band image ($C1$ filter) of the region around IRAS 17149-3916, overlapped by the IRAS error ellipse (broken line). Several stars fall inside the ellipse; a more accurate coordinate for IRAS 17149-3916 was obtained from the Midcourse Space Experiment (Price et al. 2001) - MSX⁴ point source catalog. We found one MSX source within the IRAS error ellipse (G348.2362-0.9809), with coordinates $\alpha(\text{J2000}) = 17^{\text{h}}18^{\text{m}}25.2^{\text{s}}$, $\delta(\text{J2000}) = -39^{\text{d}}19^{\text{m}}42^{\text{s}}$, which is shown as a contour diagram in Figure 6. None of the stars coincides with the MSX coordinates. In fact, from figure 6, we can see that probably several individual sources can be contributing to the IRAS emission.

3.3. $\text{Br}\gamma$ emission from the infrared nebula

As we already mentioned, there is a strong and compact (with about 1 arcmin radius) radio source in the direction of IRAS17149-3916 (PMNJ 1718-3918), with a flux density of 11.9 Jy at 4.85GHz. In order to study this extended emission, we re-observed in the 2005 observing run, the field toward IRAS17149-3916 source through the narrow band K filters, which are centered in the $\text{Br}\gamma$ line and in the adjacent continuum (see table 1).

To calculate the total $\text{Br}\gamma$ emission, we first scaled the counts of the continuum image ($C1$ filter) to the same level of the $\text{Br}\gamma$ image, using the common bright field stars. In Figure 7, we show the $\text{Br}\gamma$ contour diagram constructed from the difference between the $\text{Br}\gamma$ and $C1$ images, overlaying the Spitzer⁵ $3.6\mu\text{m}$ image of the region around IRAS17149-3916; we also indicated the position of four prominent Spitzer sources coincident with the infrared objects IRS1, IRS2, IRS3 and IRS4 from our survey. From that figure, we can also see that the $\text{Br}\gamma$ emission presents a "shell" like shape, which seems to be enclosed by $3.6\mu\text{m}$ dust emission. From the spectral type of IRS1 (O5V-O6V derived from the color-magnitude diagram in figure 5), which is the most luminous source in the whole region, we can speculate that the observed $\text{Br}\gamma$ flux density probably is generated by the

⁴<http://www.ipac.caltech.edu/ipac/msx/msx.html>

⁵<http://www.ipac.caltech.edu/data/SPITZER/SPITZER>

Table 2—Continued

IRS	$\alpha(\text{J2000})$	$\delta(\text{J2000})$	J_{CamIV}	H_{CamIV}	K_{CamIV}
93	17:18:22.1	-39:19:11.6		14.68 ± 0.05	12.89 ± 0.07
94	17:18:21.36	-39:19:54.1		15.60 ± 0.06	13.81 ± 0.11
95	17:18:30.53	-39:19:37.6		14.33 ± 0.05	13.82 ± 0.11
96	17:18:26.59	-39:17:56.8		13.98 ± 0.05	13.37 ± 0.09

same ionized gas that produces the free-free emission detected at radio wavelengths.

Next we constructed the flux calibrated contour diagrams of the two images (the Br γ and C1 contour diagrams) and, by measuring the area between contours, we obtained the net Br γ flux density using the relation between magnitude and flux density given by Koorneef (1983), finding an integrated Br γ flux density of $7.1(\pm 1.1) \times 10^{-11}$ erg cm $^{-2}$ s $^{-1}$.

3.4. Mean visual extinction and emission measure determined from the Br γ and radio flux densities

To estimate the mean visual extinction A_V in the direction of the nebula, we first used the integrated Br γ flux density, uncorrected for reddening, to compute the corresponding number of Lyman continuum photons, using the expression derived by Ho (1990):

$$N_{Ly} = 2.9 \times 10^{45} \left(\frac{D}{\text{kpc}} \right)^2 \left(\frac{3S_{\text{Br}\gamma}}{10^{-12} \text{ erg cm}^{-2} \text{ s}^{-1}} \right) \text{ s}^{-1} \quad (1)$$

We obtained $(1.58 \pm 0.25) \times 10^{48}$ photons s $^{-1}$. We compared this result with that derived from the 6 cm flux density, using the relation from Armand et al. (1996), assuming an electron temperature $T_e = 7500K$:

$$N_{Ly}(6 \text{ cm}) = 5.25 \times 10^{48} \left(\frac{D}{\text{kpc}} \right)^2 T^{-0.45} S_{5\text{GHz}} (\text{Jy}) \text{ s}^{-1} \quad (2)$$

We found $N_{Ly}(6\text{ cm}) = 5.25 \times 10^{48}$ photons s^{-1} , which corresponds to a mean visual extinction $A_V = 5.49 \pm_{1.32}^{2.96}$ magnitudes. This result agrees with that obtained from the color-magnitude diagram for the IRS1 source (see fig.4), which appears reddened by about $A_V \simeq 6.5$ mag.

We calculate the emission measure E from the detected 5 GHz flux density, using the observed size of the $\text{Br}\gamma$ extended emission (about 55 arcsec) and the expression of the expected free-free emission from an optically thin plasma at wavelength λ , given by:

$$S_\nu = 5.4 \times 10^{-16} g_{ff}(\lambda, T) \Omega E T^{-1/2} e^{-hc/\lambda kT} \text{ Jy} \quad (3)$$

where E is the emission measure (cm^{-5}), Ω the solid angle of the source and $g_{ff}(\lambda, T)$ the Gaunt factor, which for radio wavelengths can be calculated from:

$$g_{ff}(\lambda, T) = \frac{\sqrt{3}}{\pi} \left[17.7 + \ln \left(\frac{T^{3/2} \lambda}{c} \right) \right]. \quad (4)$$

Assuming $T=7500\text{K}$ and $S_\nu=11.9$ Jy we found $E = 4.5 \times 10^{24} \text{cm}^{-5}$, which results in a mean electron density $n_e = 2.6 \times 10^3 \text{cm}^{-3}$, characteristic of compact HII regions (Churchwell 2002).

3.5. The IRS4 near infrared source

In figure 7, we indicated the counterparts of the IRS1, IRS2, IRS3 and IRS4 sources in the $3.6\mu\text{m}$ Spitzer image. As we have already mentioned, IRS1 is the best candidate to be the main ionizing source in the cluster. The other three NIR sources present large excess of emission in the color-color diagram, appearing also as very bright IR sources in the $3.6\mu\text{m}$ image.

We attributed the excess emission from IRS2 and IRS3 to dust that probably surrounds these young stars. In the case of IRS4, we found a residual in the difference between the point spread function photometry ($\text{Br}\gamma - C1$), showing the presence of $\text{Br}\gamma$ line emission, suggesting the presence of a highly embedded UCHII region. This can be seen in Figure 8, where we present the $K(\text{Br}\gamma) - K(C1)$ versus K magnitude diagram, constructed from the point spread function photometry of the 41 common bright stars ($K \leq 11.5$) in the $\text{Br}\gamma$ and $C1$ narrow band images. From that figure we can see that all stars but one (IRS4) have compatible K photometry, considering the photometric errors.

4. Conclusions

NIR observations in the direction of RCW121 reveals the presence of a young cluster of massive stars embedded in an HII region coincident with IRAS17149-3916 source. These observations, together with published radio data, MSX and Spitzer images were used to determine some of the

physical parameters of the region. We found 96 cluster member candidates in an area of about 1.5×2.0 square arcmin, 30% of them showing excess emission in the NIR. IRS 1, the strongest source in the cluster with an estimated spectral type of O5V-O6V ZAMS based on the color-magnitude diagram, is probably the main ionizing source of the HII region detected at radio wavelengths.

We did not find a star directly associated with the MSX source coordinates; in fact, probably more than one NIR source could be heating the dust, since the strongest of them are concentrated near the maximum of the $8.28 \mu\text{m}$ emission in the MSX image. This result is different from that obtained by Roman-Lopes et al. (2003); Roman-Lopes & Abraham (2004a,b), in which a single and strong NIR source have coordinates that agree with the MSX source.

From narrow band $\text{Br}\gamma$ and continuum images we measured an extended $\text{Br}\gamma$ flux density of $(7.1 \pm 1.1) \times 10^{-11} \text{ erg cm}^{-2} \text{ s}^{-1}$. We found that the $\text{Br}\gamma$ emission presents a shell-like structure, which seems to be enclosed by $3.6 \mu\text{m}$ dust emission. Using the integrated $\text{Br}\gamma$ flux density, uncorrected for reddening, we computed the corresponding number of Lyman continuum photons and compared it with that obtained from the 5 GHz flux density to derive a mean visual extinction of $A_V = 5.49 \pm_{1.32}^{2.06}$ magnitudes. This result agrees with that inferred from the color-magnitude diagram for the IRS1 source, which appears reddened by about $A_V \simeq 6.5$ mag. From the observed size of the $\text{Br}\gamma$ extended emission and the detected 5 GHz flux density, we calculated emission measure $E = 4.5 \times 10^{24} \text{ cm}^{-5}$ and electron density $n_e = 2.6 \times 10^3 \text{ cm}^{-3}$, characteristic of compact HII regions Churchwell (2002). Moreover, the IRS4 object presents a residual in the difference between the point spread function photometry ($\text{Br}\gamma - C1$), showing the presence of $\text{Br}\gamma$ line emission, suggesting the existence of a highly embedded UCHII region.

Acknowledgments

This work was partially supported by the Brazilian agencies FAPESP and CNPq. We acknowledge the staff of Laboratório Nacional de Astrofísica for their efficient support. This publication makes use of data products from the Two Micron All Sky Survey, which is a joint project of the University of Massachusetts and the Infrared Processing and Analysis Center/California Institute of Technology, funded by the National Aeronautics and Space Administration and the National Science Foundation. This research made use of data products from the Midcourse Space Experiment. This work is based [in part] on observations made with the Spitzer Space Telescope, which is operated by the Jet Propulsion Laboratory, California Institute of Technology under a contract with NASA.

REFERENCES

Armand, C., Baluteau, J.-P., Gry, C., Cox, P. 1996, A&A, 306, 593

- Bromfmann, L., Nyman, L-Å, May, J., 1996, A&A, 115,81
- Caswell, J. L., Haynes, R. F. 1987, A&A, 171, 261
- Cesaroni, R., Walmsley, C.M., Kompe, C., Churchwell, E. 1991, A&A, 252, 278
- Churchwell, Ed 1990, A&A, 2,79
- Churchwell, Ed 2002, ARA&A,40,27
- Cohen, R. J., Mashedier, M. R. W., Caswell, J. L. 1995, MNRAS, 274, 808
- Dutra, C. M., Bica, E., Soares, J., Barbuy, B. 2003, A&A, 400, 533
- Fitzpatrick, E. L. 1999, PASP, 111, 63
- Hanson, M. M., Howarth, I. D., Conti, P. S. 1997, ApJ, 489, 718
- Hanson, M.M., Luhman, K.L., Rieke, G.H. 2002 ApJS, 138, 35
- Ho, Paul T. P.; Beck, Sara C.; Turner, Jean L. 1990 ApJ, 349,57H
- Koornneef, J. 1983, A&A, 128, 84
- Lada, C. J., Adams, F. C. 1992, ApJ, 393, 278
- Mezger, P.G. & Henderson, A.P. 1967, ApJ, 147, 471
- Price, S. D., Egan, M. P., Carey, S. J., Mizuno, D. R., Kuchar, T. A. 2001, AJ, 121, 2819
- Rodgers, A. W., Campbell, C. T., Whiteoak, J. B. 1960, MNRAS, 121, 103
- Roman-Lopes, A., Abraham, Z., Lépine, J. R. D. 2003, AJ, 126, 1896
- Roman-Lopes, A., Abraham, Z. 2004a, AJ, 127, 2817
- Roman-Lopes, A., Abraham, Z. 2004b, AJ, 128, 2364
- Roman-Lopes, A., Abraham, Z. 2005, AJ, submitted
- Walsh, A. J., Burton, M. G., Hyland, A. R., Robinson, G. 1997, MNRAS, 291, 261
- Wood, D. O. S., Churchwell, E. 1989, ApJ, 340, 265

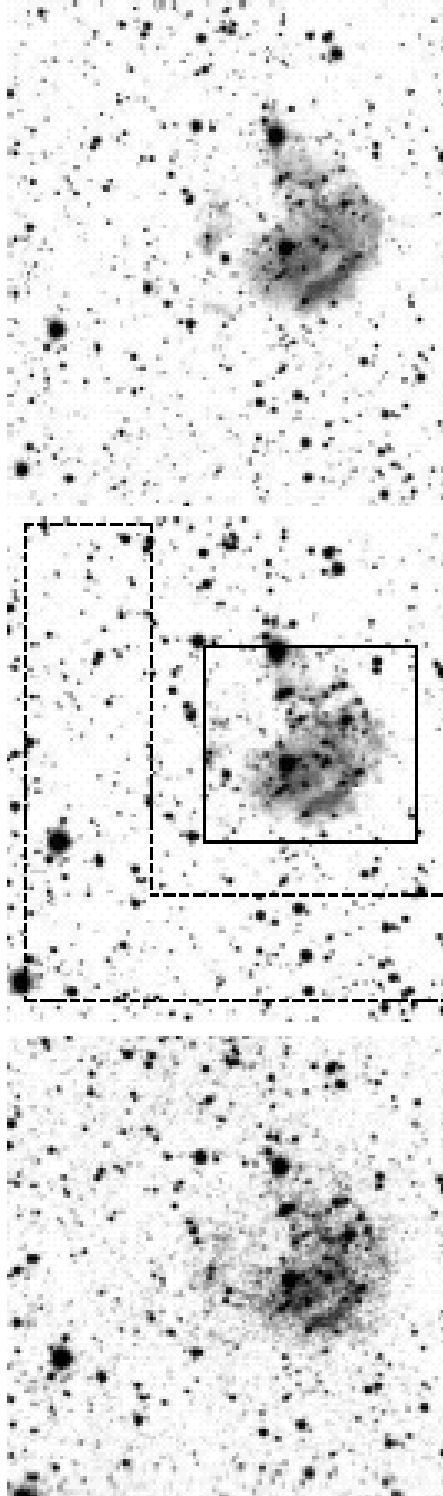


Fig. 1.— The J (up), H (center) and $K(C1)$ (down) infrared images (about $5.2' \times 5.6'$). These frames were taken using the near infrared camera coupled to the 0.6 m Boller & Chivens telescope, during the 2003 observing run. North is to the top, east to the left. The "cluster" and "control" regions are indicated by the dashed and solid lines, respectively.

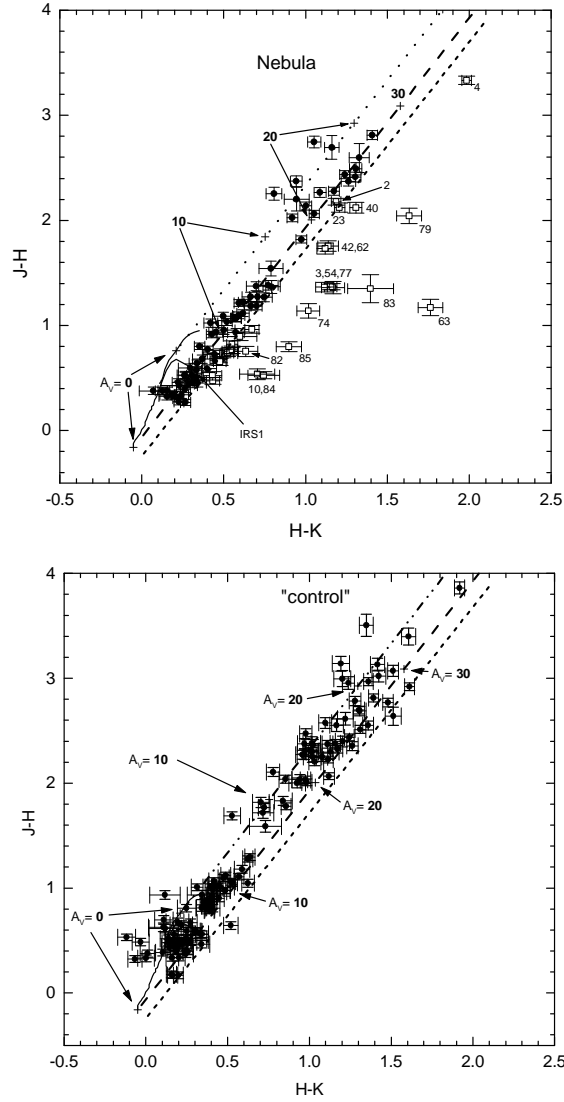


Fig. 2.— Color-color diagrams for two comparative regions in our survey. The control diagram probably contains only field objects; the nebula diagram has also some field stars but presents many young objects with excess emission in the NIR. The locus of the main sequence and the giant branch are represented by the solid lines (Koornneef,1983), while the reddening vector for late and early type stars are represented by dotted and long dashed lines respectively. A third vector represented by the long dotted line indicate the place in the color-color diagram where the stars present excess emission in the NIR.

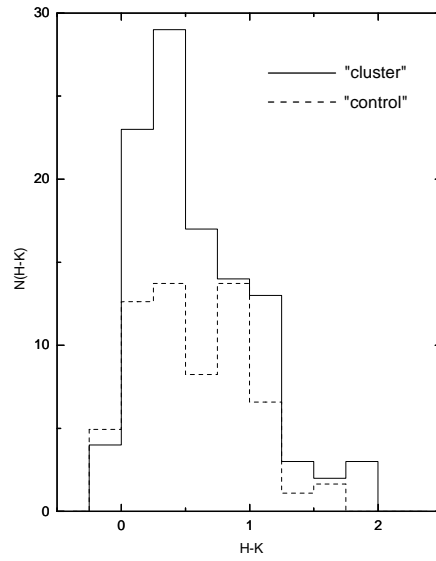


Fig. 3.— Comparative histogram of the distribution of the $H - K$ colors in the control (dashed line) and in the cluster (solid line) regions. The counts of the control area were normalized to the area of the cluster region.

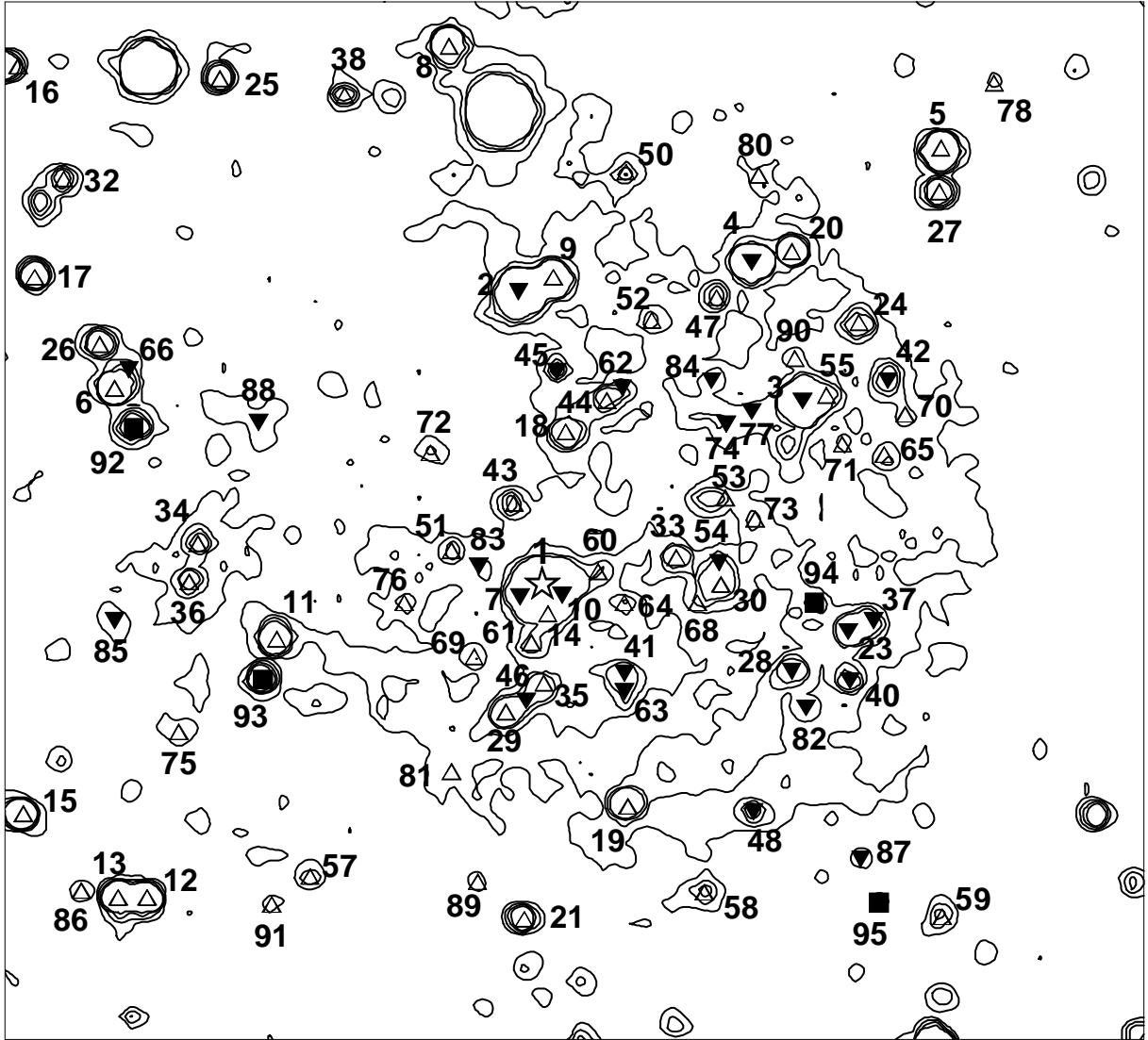


Fig. 4.— nbK-band contour diagram of the infrared nebula region. The contours are spaced in intervals of 10%, 40%, 80% and 100% of the peak value. Here we indicate the position of the sources with excess emission (filled triangles), those without (open triangles), the main ionizing source candidate (star), and those only detected at *H* and *K* bands (filled squares).

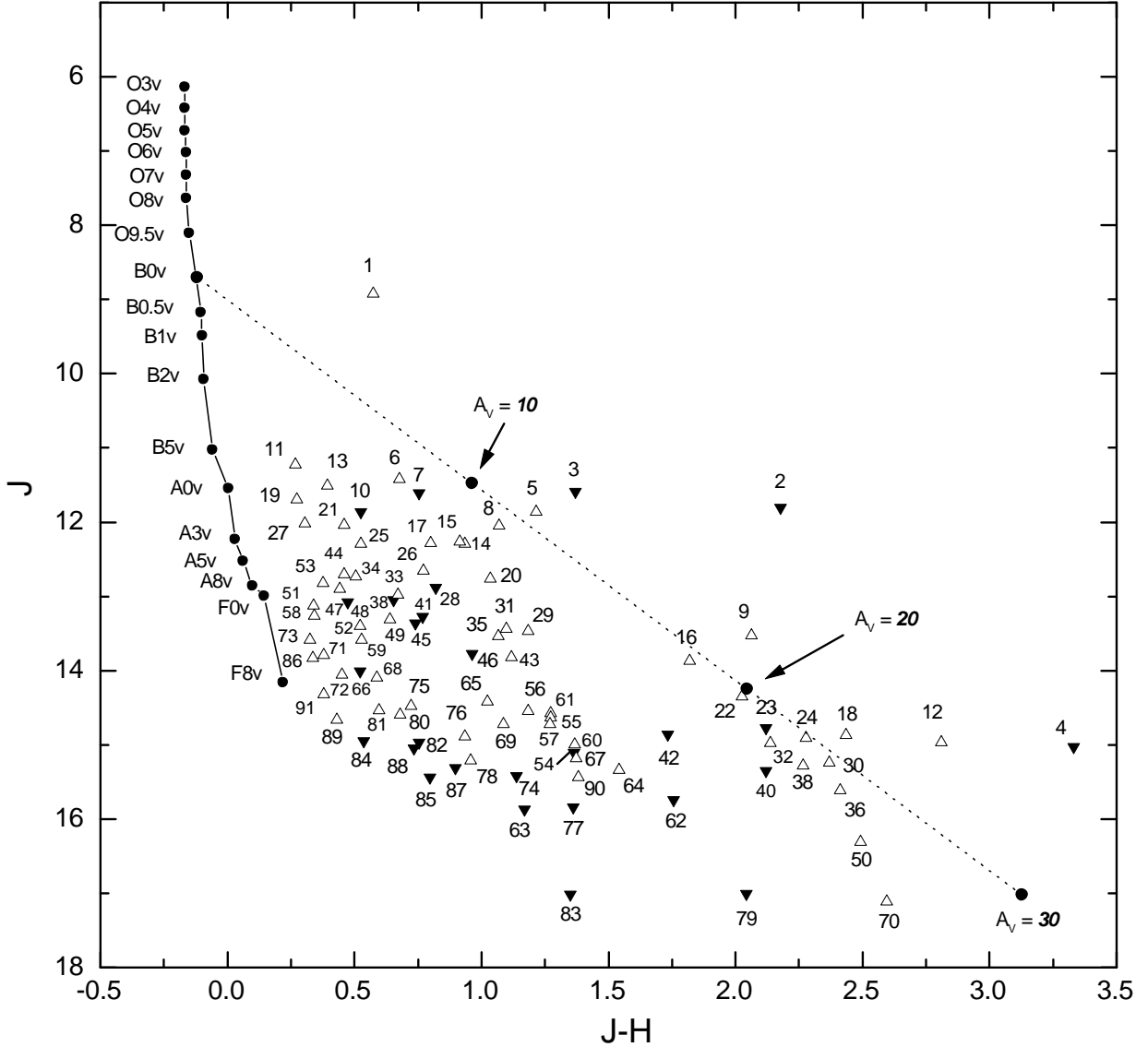


Fig. 5.— The J vs $J - H$ color-magnitude diagram of the sources in Table 1. The locus of the main sequence at 1.6 kpc is shown by the solid line. The intrinsic colors are from Koornneef (1983), while the absolute J magnitudes were calculated from Hanson et al. (1997). The reddening vector for a B0 ZAMS star (*dotted line*) is from Fitzpatrick (1999). We also indicate the location (*bold numbers*) of $A_V = 10, 20$ and 30 mag of visual extinction as well as the sources that show excess (filled triangles) and those that do not (open triangles) in the color-color diagram.

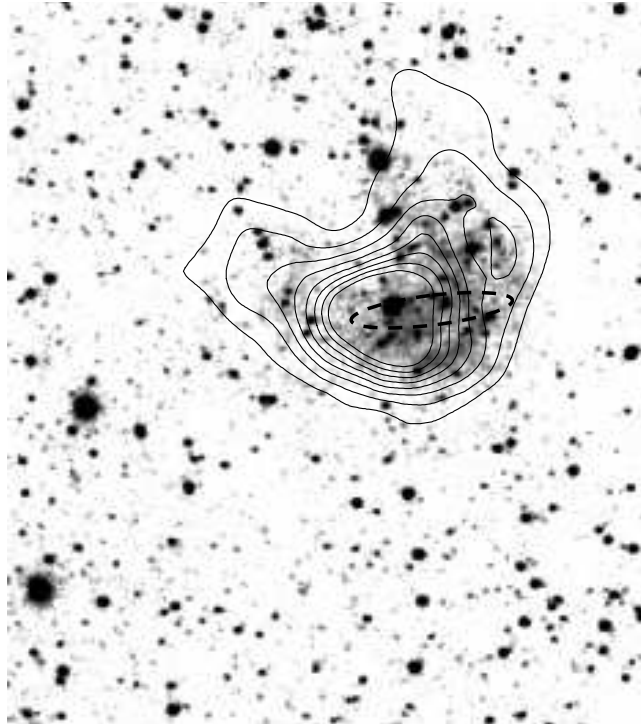


Fig. 6.— Contour diagram from the MSX A-band image ($8.28 \mu\text{m}$), overlaid by the LNA *C1* image. The IRAS coordinate error ellipse is represented by the dashed ellipse.

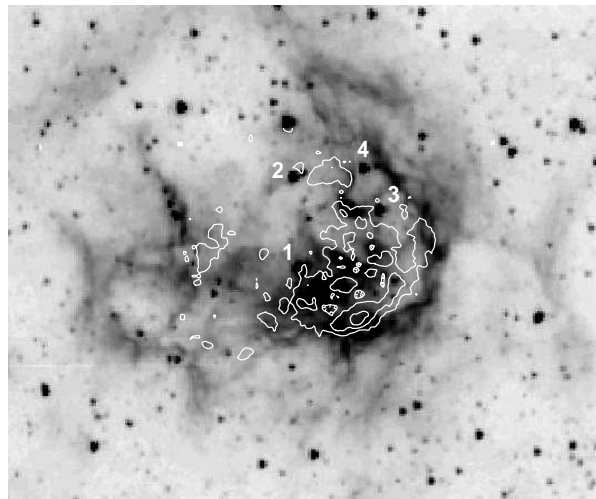


Fig. 7.— Contour $\text{Br}\gamma$ diagram overlaid by the Spitzer $3.6\mu\text{m}$ image of the region around IRAS17149-3916. The contours start at $695 \text{ counts arcsec}^{-1}$ and are spaced by the same value.

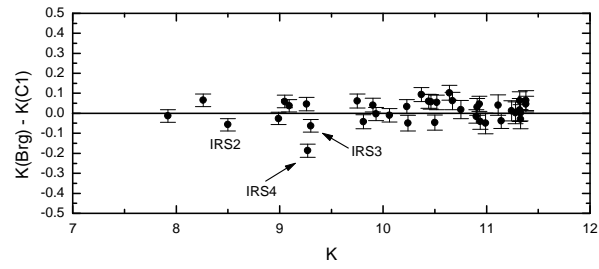


Fig. 8.— The $K(\text{Br}\gamma)$ - $K(\text{C}1)$ versus K magnitude diagram, constructed from the PSF photometry of 41 common bright stars ($K \leq 11.5$). The anomalous source in this diagram corresponds to the IRS4 source (see text).